

Reduced defect density in crystalline halide perovskite films via methylamine treatment for the application in photodetectors

Cite as: APL Mater. 10, 081110 (2022); <https://doi.org/10.1063/5.0093333>

Submitted: 28 March 2022 • Accepted: 01 August 2022 • Published Online: 26 August 2022

 Emilia R. Schütz,  Azhar Fakharuddin, Yenal Yalcinkaya, et al.



View Online



Export Citation



CrossMark

ARTICLES YOU MAY BE INTERESTED IN

[Spatial post-filter for linear hydrophone arrays with applications to underwater source localisation](#)

JASA Express Letters 2, 084802 (2022); <https://doi.org/10.1121/10.0013753>

[Effects of amplitude modulated discharge on growth of nanoparticles in TEOS/O₂/Ar capacitively coupled plasma](#)

AIP Advances 12, 085220 (2022); <https://doi.org/10.1063/5.0097691>

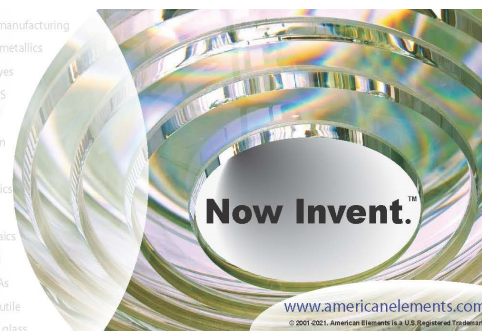
[Preface: Proceedings of the International Conference on recent advances in manufacturing engineering research \(ICRAMER 2021\)](#)

AIP Conference Proceedings 2460, 010001 (2022); <https://doi.org/10.1063/12.0010326>



yttrium iron garnet glassy carbon beamsplitters fused quartz additive manufacturing
zeolites III-IV semiconductors gallium lump copper nanoparticles organometallics
nano ribbons barium fluoride europium phosphors photonics infrared dyes
epitaxial crystal growth ultra high purity materials transparent ceramics CIGS
cerium oxide polishing powder surface functionalized nanoparticles MRE grade materials thin film
sapphire windows Nd:YAG silver nanoparticles perovskites OLED lighting solar energy
rare earth metals quantum dots osmium scintillation Ce:YAG sputtering targets fiber optics
refractory metals laser crystals h-BN deposition slugs CVD precursors photovoltaics
anode lithium niobate InAs wafers dysprosium pellets MOFs AuNPs metaperiodics borosilicate glass
chalcogenides ZnS CdTe YBCO superconductors InGaAs
perovskite crystals transparent ceramics diamond micropowder optical glass

The Next Generation of Material Science Catalogs



Reduced defect density in crystalline halide perovskite films via methylamine treatment for the application in photodetectors

Cite as: APL Mater. 10, 081110 (2022); doi: 10.1063/5.0093333

Submitted: 28 March 2022 • Accepted: 1 August 2022 •

Published Online: 26 August 2022











View Online



Export Citation



CrossMark

Emilia R. Schütz,¹  Azhar Fakhruddin,¹  Yenal Yalcinkaya,^{2,3} Efrain Ochoa-Martinez,⁴  Shanti Bijani,⁵ 
Abd. Rashid bin Mohd Yusoff,⁶  Maria Vasilopoulou,⁷ Tobias Seewald,¹  Ullrich Steiner,⁴ 
Stefan A. L. Weber,^{2,3} and Lukas Schmidt-Mende^{1,a)} 

AFFILIATIONS

¹ Department of Physics, University of Konstanz, D-78457 Konstanz, Germany

² Max Planck Institute for Polymer Research, Ackermannweg 10, 55128 Mainz, Germany

³ Institute of Physics, Johannes Gutenberg University Mainz, Duesbergweg 10-14, 55128 Mainz, Germany

⁴ Adolphe Merkle Institute, University of Fribourg, Chemin des Verdiers 4, 1700 Fribourg, Switzerland

⁵ Unidad de Nanotecnología, Centro de Supercomputador y Bioinnovación SCBI, Universidad de Málaga, Calle Severo Ochoa 34, 29590 Campanillas (Málaga), Spain

⁶ Department of Chemical Engineering, Pohang University of Science and Technology (POSTECH) 77 Cheongam-Ro, Nam-Gu, Pohang 37673, Republic of Korea

⁷ Institute of Nanoscience and Nanotechnology, National Center for Scientific Research "Demokritos," 15341 Agia Paraskevi, Attica, Greece

^{a)} Author to whom correspondence should be addressed: Lukas.Schmidt-Mende@uni-konstanz.de

ABSTRACT

Considerable efforts have been devoted to optimizing and controlling the morphology and electronic properties of lead halide perovskites. The defect density of a perovskite layer strongly depends on the processing conditions. Consequently, the fabrication process of high-quality films is often complex, and reproducibility is a challenge. In this work, we present a methylamine gas-based method to recrystallize perovskite layers of any given quality in a controlled way, leading to millimeter-sized domains. Crystallinity significantly increases upon methylamine treatment, and crystal growth follows a preferred orientation. Photoluminescence- and space-charge limited current measurements show that the trap density halves after recrystallization. Conductive atomic force microscopy measurements show a higher surface conductivity and an improved spatial homogeneity after methylamine treatment. When applied in photodetectors, the improved film quality of the recrystallized films leads to increased detectivities of $\approx 4 \times 10^{11}$ Jones compared to 3×10^9 Jones of a reference device. The response time falls from 0.1 to 10^{-5} s upon methylamine treatment. Our work, thus, presents a promising route to fabricating reproducible, high-quality perovskite films through well-controllable recrystallization.

© 2022 Author(s). All article content, except where otherwise noted, is licensed under a Creative Commons Attribution (CC BY) license (<http://creativecommons.org/licenses/by/4.0/>). <https://doi.org/10.1063/5.0093333>

I. INTRODUCTION

Organic-inorganic hybrid perovskite materials are currently achieving breakthroughs in a range of optoelectronic devices due to their unique properties.¹⁻⁴ These include their low defect density and high defect tolerance,⁵⁻⁷ the facile bandgap⁸⁻¹⁰ and

nanocrystal size¹¹ tuning, and high charge carrier mobilities in the range of 1–30 cm²/Vs.¹²⁻¹⁴ As these materials are commonly processed from solution and their crystallization completes within time spans of several seconds up to a few minutes, the fabrication process is very delicate.^{15,16} Extreme care is necessary for developing high-quality perovskite films. Uncontrolled growth of perovskite crystals

leads to the formation of defects due to compositional and structural disorder, which significantly limit device performance.^{17,18} Surface defects in perovskite films, including those at grain boundaries (GBs), are well-known,¹⁸ and high-efficiency devices often employ surface passivation techniques to reduce the defect density.^{17,19}

Since the emergence of halide perovskites, efforts have, therefore, been dedicated to engineering their film morphology. Irrespective of the ongoing debate whether large or small grains are desirable for high-efficiency devices, the GBs, if not effectively passivated, act as defect sites leading to a non-radiative recombination.²⁰ GBs have also shown to be sites of moisture ingress and are, thus, among the primary sources of device instability.²¹ This is why several strategies to fabricate large perovskite grains have been introduced. Some notable methods include hot casting,^{22,23} optimizing the reaction temperature of perovskite annealing,²⁴ template-assisted growth,^{25–27} thermal and solvent treatments,^{28,29} and the effect of substrate layers.^{30,31} Note that these methods add complexity to the device fabrication process and that not all of them are compatible with large-area processing.

Methylamine (MA⁰) gas-based post-treatments present a different approach to improving the morphology and crystallinity of perovskite films.³² They are based on the interaction between MA⁰ and hybrid organic–inorganic perovskites first reported by Zhou *et al.*³³ When exposed to the MA⁰ gas, the perovskite phase readily collapses into a liquid intermediate phase,³⁴



The causes of this interaction are thought to be the disruption of the bonds in the PbI₆ octahedral lattice due to bonding of the MA⁰ with lead (Pb²⁺) and methylammonium (MA⁺) ions.^{35,36}

In principle, two different routes to recrystallization have been explored. When the MA⁰ atmosphere is removed, the film recrystallizes and forms a smooth, fine-grained film. Improved surface coverage, crystallinity, and vastly improved solar cell performance compared to raw films have been achieved this way.^{33,37} The other method, first shown by Jacobs and Zang,³⁸ relies on heating the sample without removing the MA⁰ gas. At elevated temperatures, crystal seeds form and grow outward, forming large domains. Such films exhibit increased crystallinities^{38,39} and have successfully been implemented in high-performing solar cells by Fan *et al.*³⁹ Irrespective of the recrystallization method, the crystal phase reforms during the treatments, its properties depending only on the atmospheric conditions. In consequence, these post-deposition treatments could provide the means to decouple the film quality from the initial deposition process and, therefore, are promising to improve reproducibility, facilitate upscaling, and lower production costs. As they open up the opportunity to reduce or even eliminate the influence of GBs in film degradation due to the increased grain size, such MA⁰-gas treatments also show great promise regarding the stability of fabricated devices.

We herein present a new MA⁰-based treatment protocol and setup with which we can obtain mixed triple cation perovskite films with near-millimeter domain size. We show drastically improved crystallinities, as evidenced by x-ray diffraction (XRD) intensities increasing by orders of magnitude in the recrystallized films. In addition, space-charge limited current (SCLC) measurements show a reduction of the trap densities from 8×10^{16} to $4 \times 10^{16} \text{ cm}^{-3}$

after MA⁰ treatment, resulting in strongly improved photodetection devices, with the specific detectivities increasing from $\approx 3 \times 10^9$ to 4×10^{11} Jones.

II. RECRYSTALLIZING PEROVSKITE FILMS IN A METHYLAMINE ATMOSPHERE

Precise control over the amount of MA⁰ gas to which the samples are exposed as well as over the temperature and exposure times, allowing us to systematically vary and optimize all parameters during exposure and recrystallization. The setup and processing conditions are described in further detail in the [supplementary material](#) (see Fig. S1).

We found that at a given MA⁰ partial pressure p_{MA} , the perovskite film only collapses into a liquid state when below a temperature T_{rec} . Above this transition temperature, the material is solid in equilibrium despite a persisting MA⁰ atmosphere. Determining these temperatures, T_{rec} for different p_{MA} gives a rough phase p–V diagram shown in Fig. 1(a). Note that these values were determined for a mixed triple-cation perovskite [Cs_{0.1}(MA_{0.17}FA_{0.83})_{0.9}Pb(I_{0.83}Br_{0.17})₃], but an equivalent behavior is observed in MAPbI₃.

Taking advantage of this knowledge, we have developed a MA⁰ treatment protocol that reliably yields large grains grown in a controlled fashion. In contrast to previous studies,^{38,39} we choose to keep the temperature constant throughout the entire process and instead lower the partial pressure to initialize recrystallization. As the heating process often takes minutes, during which the film may or may not start crystallizing, and the heating rate varies with external conditions, the MA⁰ treatment becomes faster and more predictable this way.

We start with the sample at an elevated temperature T , which is kept constant. After establishing an inert nitrogen atmosphere, a certain amount of MA⁰ gas is led into the chamber up to a MA⁰ partial pressure p_{MA} . If T is smaller than the recrystallization temperature $T_{\text{rec}}(p_{\text{MA}})$ at this initial partial pressure, the film collapses into the liquid phase. To initialize recrystallization, the partial pressure inside the reaction chamber is then lowered by gradually evacuating the chamber. As the transition is crossed as indicated by the arrow in Fig. 1(a), recrystallization starts in the form of seed nuclei. These crystals slowly grow until the entire substrate is covered with large grains.

By choosing a combination of pressures and temperatures where we move to a point in the phase diagram just barely above the recrystallization temperature after evacuation, we can achieve very slow nucleation and grain growth, resulting in nearly millimeter-sized grains. The higher the temperature difference $T - T_{\text{rec, new}}$ (i.e., the greater the vertical distance from the transition line in the phase diagram), the faster the crystallization process becomes and the smaller the resulting grains (see Fig. S2). We, thus, also gain control over the mean grain size by controlling the recrystallization temperature.

Figure 1(b) shows the top-view optical microscopy images of the nucleation and growth of individual grains. It is clearly visible how individual grains nucleate and symmetrically grow outward. The growth process itself takes several minutes and ends when neighboring grains meet to form a continuous film.

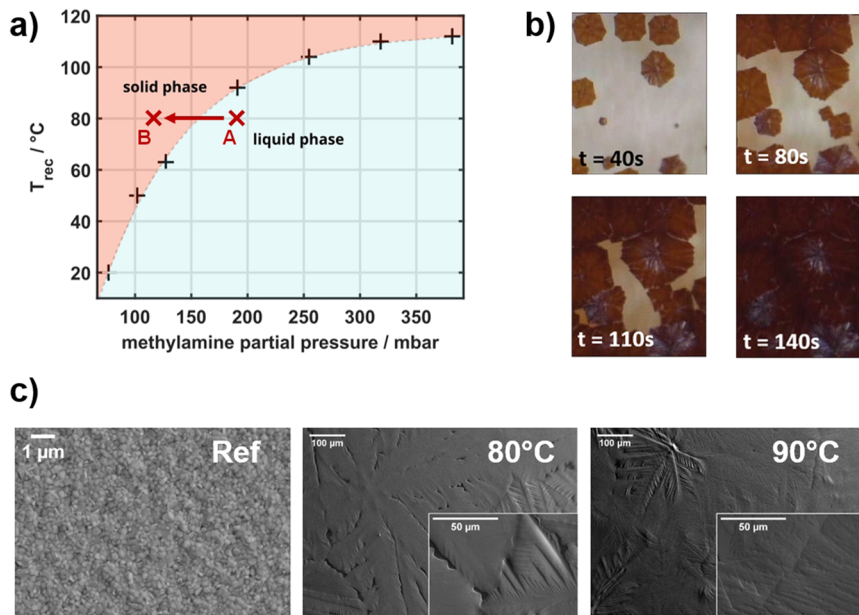


FIG. 1. (a) Transition temperatures T_{rec} for different MA⁰ partial pressures inside the chamber. The dotted line guides the eye along the transition line between the solid and the liquid state. During the process, the MA⁰ partial pressure is lowered along the red arrow from the exemplary point A to point B. As the transition line is crossed during this process, recrystallization is induced. (b) The recrystallization process after nucleation, as observed through a microscope camera from above. (c) Scanning electron microscopy (SEM) topographies of the anti-solvent reference and the MA⁰ treated 80 °C and 90 °C films.

We have applied this process to a mixed triple-cation perovskite to investigate the resulting film properties. The perovskite layer was deposited on indium tin oxide (ITO)/tin(II) oxide (SnO₂) substrates. An untreated reference film was compared to the recrystallized samples throughout this work. We used a MA⁰ partial pressure of ~230 mbar, which was then reduced to 170 mbar through pumping. We found that for these pressures, the samples can be liquefied and recrystallized if the sample temperature T lies between roughly 80 and 100 °C. At the lower end of this range, the resulting recrystallization process is slow and takes up to 30 min. While the recrystallization process is much faster at higher temperatures, the liquefaction is only very brief or partial above 100 °C, leading to an incomplete film transformation. We have chosen two temperatures T within this range, 80 °C and 90 °C, and have characterized the resulting film properties, which we discuss below.

III. FILM MORPHOLOGY, CRYSTALLINITY, AND COMPOSITION

Figure 1(c) shows scanning electron microscopy (SEM) images of an as-deposited reference film and the recrystallized films after MA⁰ treatment at 80 and 90 °C. The surface of the reference film is very uniform and smooth, and individual grains with diameters on the order of tens of nanometers are visible. In contrast, domains of several hundred micrometers in diameter are visible after MA⁰ treatment. For these slowly grown grains, one can clearly discern their point of origin, where nucleation in the liquid phase first occurred, and structures that radiate outward in the direction of crystal growth. The main difference between the samples at 80 and 90 °C lies in how different grains meet at their edges to form boundaries. In the 80 °C films, gaps and holes are apparent at the domain boundaries, whereas in the 90 °C films, the individual domains meet almost seamlessly.

One possible explanation for this observation is the long crystallization times at 80 °C. Similar to observations made in conventional perovskite film fabrication from solvent-based precursors,^{40,41} the liquid phase on the substrate tends to de-wet from the surface. In the moment of liquefaction, when the solid phase collapses, the substrate is still fully covered. As recrystallization starts, however, crystals partially replace the liquid areas. At the edges of the growing grains, holes in the films start to become energetically favorable. If the recrystallization process is too slow and the film has enough time to de-wet, gaps may form between different grains. At a higher recrystallization temperature, the crystals grow much faster and meet at their boundaries before the liquid has had time to locally de-wet.

It is worth noting that no substructures comparable to the grains in the reference are resolved in the MA⁰ treated films. The visible planes appear to be perfectly flat in the SEM images (see Fig. S3). Atomic force microscopy (AFM) topographies [see Figs. 5(b) and 5(d)] do show a smaller substructure on the order of tens of micrometers, which are still orders of magnitude larger than the reference grain size. In addition, electron backscattering diffraction studies (see Fig. S4) show that the recrystallized film is oriented in one crystallographic direction within individual domains. We, therefore, conclude that the slow growth from the liquid intermediate resembles the growth of single crystals from solution and leads to large crystalline domains.

To corroborate these observations, we obtained XRD spectra of the films [Fig. 2(a)]. The peak intensities of the (110)-peak have been extracted and are shown in Fig. 2(b).

The results, indeed, show that the MA⁰ treatment produces highly crystalline films with a (110) out-of-plane orientation. In contrast, the reference sample shows orders of magnitude lower XRD peak intensities and differently oriented phases, indicating a distribution of small and randomly oriented crystallites. A careful analysis of the (110) diffraction peak in Fig. 2(c) shows a shift to

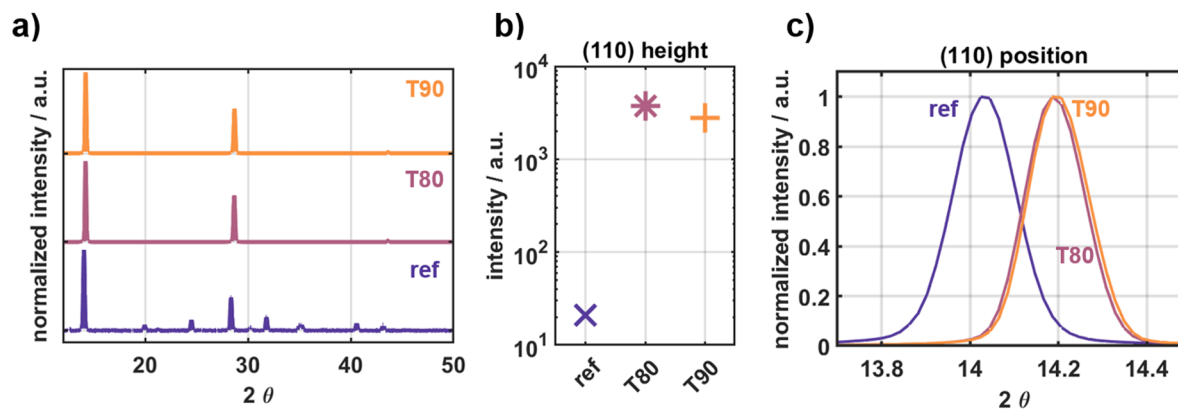


FIG. 2. (a) XRD patterns obtained for reference and MA⁰ treated samples, recrystallized at different temperatures. (b) Comparison of (110) peak intensity for the different samples. (c) Normalized intensity for the (110) diffraction peak.

larger diffraction angles upon MA⁰ treatment. This phenomenon is accompanied by a substantial shift in the photoluminescence (PL) peak position to smaller wavelengths of around 30 nm from 760 to 732 nm after MA⁰ treatment (see Fig. S5). Equivalent observations of a shift in the optical bandgap were made by ultraviolet–visible (UV–vis) spectroscopy measurements (see Figs. S6 and S7 and Table SI). There are two possible explanations for this behavior: an increase in macrostrain⁴² or compositional changes. A partial exchange of formamidinium (FA⁺) for MA⁺ in the perovskite lattice could explain the peak shifts^{43,44} and is plausible, considering the exposure of the film to MA⁰ gas. Similar gas-induced compositional transformations have been demonstrated before.^{45–47} The hypothesis of a compositional change is supported by x-ray photoelectron spectroscopy (XPS) measurements showing a decreased relative amount of nitrogen in the films after MA⁰ treatment (see the [supplementary material](#), Tables SII and SIII as well as Figs. S8 and S9, for more details). The Williamson–Hall analysis of our data (see Fig. S10 and Table SIV), on the other hand, shows that there is, indeed, increased microstrain in the film. The shifts in the XRD peak position and bandgap are, thus, likely caused by a combination of both effects. The Williamson–Hall analysis also shows an increase in calculated crystallite size after MA⁰ treatment, proving a qualitative improvement in crystallite packing after recrystallization. For a more detailed discussion, see the [supplementary material](#) (Fig. S10 and Table SIV).

IV. PHOTOLUMINESCENCE AND QUANTIFICATION OF DEFECT DENSITIES

To further characterize our films, we performed PL measurements. The samples are excited with a pulsed 405 nm laser source. As mentioned above, the emission peak shifts from 760 to 734 nm and 732 nm after MA⁰ treatment at 80 and 90 °C, respectively, likely primarily due to changes in film composition and strain. We performed time-resolved PL measurements under continuous illumination to track the changes of the emission behavior during light-soaking over 20 min.

Figure 3(a) shows the PL spectra of an exemplary reference sample. We observe a slow rise in intensity, which is steep at first and later flattens. This increase is accompanied by a shift of the emission peak to larger wavelengths with prolonged illumination. This behavior is observed consistently across all spots and samples, with variations in the exact magnitude of the increase.

Individual measurements are less consistent after MA⁰ treatment. While, generally, the MA⁰ treated samples exhibit an increase in intensity and a shift to larger wavelengths, the shape and magnitude of these trends vary between different spots. To illustrate this behavior, multiple measurements are shown in Fig. S11. The observed variations can be explained by comparing the laser spot size (around 300 μm) with the perovskite domain sizes. The reference films are very fine-grained, and individual domains are several orders of magnitude smaller than the illuminated spot. The measured PL is the collective signal of multiple grains across boundaries and bulk areas alike. Structural inhomogeneity within the films is, therefore, not resolved. The resulting measurement represents the average across the entire illuminated area. In contrast, the hundreds of micrometer-sized domains of the MA⁰ treated samples are on the same scale as the laser spot size. When measuring different, randomly chosen spots on the film, the difference between growth centers, bulk areas, and boundaries will be represented in the resulting data.

Nonetheless, comparisons between the reference and MA⁰ treated samples can be made when looking at the statistics of multiple measurements. Boxplots of the PL intensity increase relative to the initial value and the total peak shift are shown in Figs. 3(b) and 3(c).

It is apparent that the total increase in intensity is much less pronounced after MA⁰ treatment. While the peak height increased 2.1-fold in the median measurement of the reference films, the median only increased 1.1-fold and 1.4-fold in the 80 and 90 °C samples, respectively. In addition, the total peak shift is less distinct and considerably less consistent after MA⁰ treatment.

The observed slow increase in PL intensity has previously been attributed to different effects: Ion migration, facilitated by the photoexcitation of the material,^{48,49} leading to a “curing” of defect states

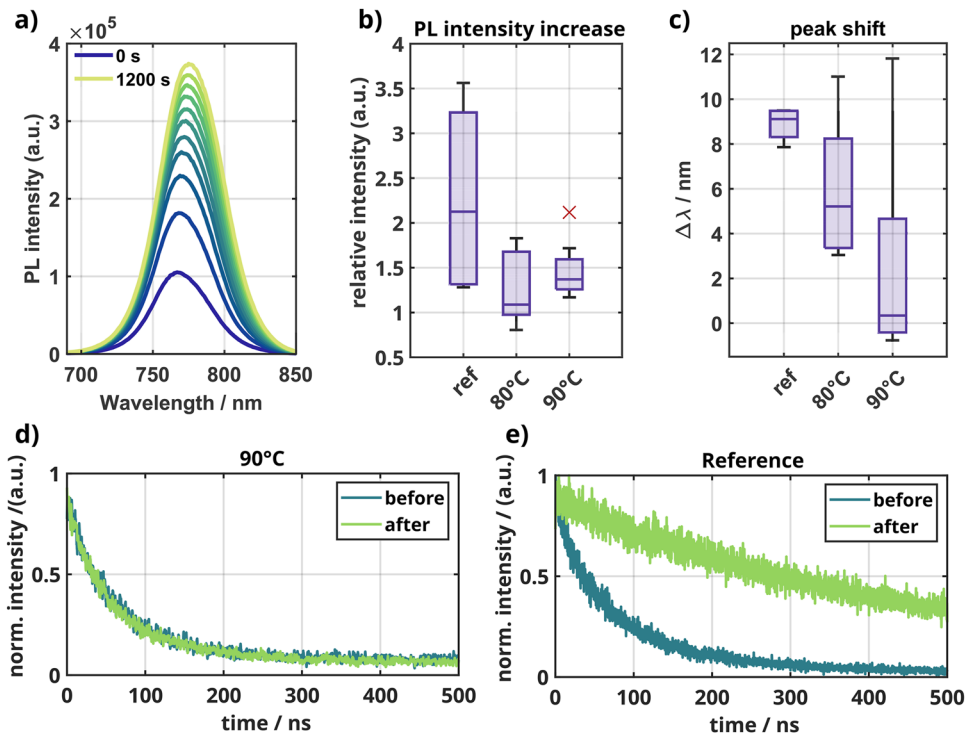


FIG. 3. (a) Exemplary PL spectra of a reference sample under continuous illumination between 0 and 1200 s. (b) Total relative intensity increase after 1200 s compared to the initial peak intensity for the reference samples and the MA⁰ treated samples after recrystallization at 80 and 90 °C. (c) Total shift of the peak position after 1200 s of continuous illumination. (d) and (e) Time-resolved photoluminescence (TRPL) of the reference and MA⁰ treated films, before and after 1200 s of continuous illumination.

upon illumination. Iodine ions, in particular, have been shown to migrate away from the site of illumination, removing defects and, thus, defect states on their way.⁵⁰ This reduces trap-assisted non-radiative recombination channels and the PL intensity increases. Furthermore, it has been shown that defect states are deactivated by photoexcited carriers more effectively in the presence of oxygen.^{51–53}

Both mechanisms have in common that pre-existing defect states in the film are deactivated through illumination. The extent of this effect is, therefore, inherently coupled to the number of trap states present in the material previous to illumination. We can thus conclude that the reduced light-soaking induced increase in PL intensity indicates a lower trap density after MA⁰ treatment. This finding is consistent with the drastically increased XRD intensity, indicating a higher degree of order in the film, and the reduced amount of boundaries and boundary defects, due to the increased grain size.

The observed shift in peak position is not commonly observed in light-soaking experiments.^{50,51,53,54} This indicates that chemical changes, such as phase segregation, are induced upon illumination in this particular mixed perovskite. As this behavior is less pronounced after MA⁰ treatment, the chemical phase stability is likely improved during the recrystallization process.

We further conducted time-resolved photoluminescence (TRPL) measurements of our ITO/SnO₂/perovskite samples before and after 1200 s of continuous illumination. Note that the fabrication of identical films on a different, non-conducting substrate would severely limit comparability due to the strong influence of the substrate material on the resulting film properties during recrystallization. The resulting decay curves are shown in Figs. 3(d)

and 3(e) for a reference and a 90 °C sample. The 80 °C samples show the same behavior as the 90 °C sample, as shown in Fig. S12. The effective lifetimes τ have been extracted from biexponential fits to the data (see the [supplementary material](#), Table SV). It is apparent that the carrier lifetime of the reference film increases drastically from 40 to 240 ns after prolonged illumination, while the decay time remains virtually unchanged in the MA⁰ treated samples.

This increase in lifetime is usually observed after light-soaking^{50,51,54} and is attributed to the same mechanism as the increase in intensity. Defect states are deactivated, leading to reduced trap-assisted recombination, increasing the total charge carrier lifetime. In our samples, we assume both the PL quenching due to charge transfer at the SnO₂ interface and trap-mediated nonradiative recombination to impact the carrier lifetime.

In the MA⁰ treated samples, the light-soaking induced changes in the trap density evidently do not affect the effective lifetime. Efficient quenching at the SnO₂/perovskite interface is the dominant process before and after light-soaking. In contrast, the lifetimes increased sixfold after illumination in the reference sample. The light-induced reduction in trap states notably affects recombination dynamics, implying that trap-assisted recombination plays a substantial role in the recombination dynamics in these films. In addition, the long lifetime after illumination, which is not reduced by quenching at the SnO₂ interface, suggests inferior charge transfer into the electron transport layer before MA⁰ treatment. Overall, the TRPL measurements, thus, indicate lower trap densities and improved charge extraction at the SnO₂ interface after MA⁰ treatment.

To further corroborate our hypothesis of fewer defects in the films after MA⁰ treatment, we performed SCLC measurements and extracted the trap densities. For this purpose, we prepared electron-only devices in the configuration ITO/SnO₂/perovskite/[6,6]-phenyl-C₆₁-butyric acid methyl ester (PCBM)/2,9-dimethyl-4,7-diphenyl-1,10-phenanthroline (BCP)/silver (Ag), as sketched in Fig. 4(a).

The theory of SCLC measurements suggests that the current J through the device is proportional to the voltage V for low voltages, $J \propto V$. Once the bias reaches the trap-filled limit at V_{TFL} , i.e., when enough charges are injected into the layer to fill the traps that are limiting the transport, the current rises sharply. Above V_{TFL} , in the space-charge limited region, the current follows a square law ($J \propto V^2$).^{55,56} The trap density is given by⁵⁵

$$N_T = V_{\text{TFL}} \cdot \frac{2\epsilon\epsilon_0}{ed^2} \quad (2)$$

using the measured values for V_{TFL} , the vacuum permittivity ϵ_0 , the perovskite dielectric constant ϵ , the film thickness d , and the elementary charge e . A film thickness $d = 370$ nm was measured in cross-sectional SEM (see Fig. S13). The dielectric constant was taken as $\epsilon = 65$, a value within the range reported for perovskites.^{57,58}

Note that we have only extracted the electron trap density here, as the fabrication of hole-only devices would require the deposition and MA⁰ treatment of equivalent perovskite films on a different p-type substrate layer. As mentioned above, the underlying surface sensitively impacts the resulting perovskite morphologies, especially after the MA⁰ treatment, compromising comparability between both approaches.

Exemplary SCLC curves are shown in Fig. 4(b). Evidently, the transition voltage V_{TFL} shifts to lower values in the MA⁰ treated films.

Note that the current density measured for the 80 °C sample is approximately two orders of magnitude higher below V_{TFL} . Considering the differences in film morphology in the SEM images from Fig. 1, we may explain this observation as follows: The 80 °C films tend to exhibit holes and gaps at the GBs. In these areas, the PCBM layer directly contacts SnO₂, resulting in a locally shorted circuit. The SCLC measurements are performed with an active area of roughly 0.133 cm², effectively integrating over the entire device area. The current density contains contributions from the

gaps, increasing the overall current density. The perovskite, however, does exhibit SCLC behavior, which leads to the abrupt current rise at V_{TFL} .

We extracted the V_{TFL} from multiple measurements and calculated the electron trap density according to Eq. (2). Boxplots of the resulting values are shown in Fig. 4(c), allowing the two following observations: First, the median trap density drops from 8.145×10^{16} to 4.309×10^{16} cm⁻³ and 4.151×10^{16} cm⁻³ after MA⁰ treatment at 80 and 90 °C, respectively, confirming our previous hypothesis.

Second, the distribution is much wider for the reference films than the recrystallized ones. The liquefaction and recrystallization steps effectively reset the film formation. Consequently, the new film properties depend only on this step, in contrast to the multiple steps and factors that influence the formation of the reference films during deposition. One can therefore infer that the MA⁰ treatment leads to an improvement in reproducibility.

From the conjunction of PL and SCLC measurements, we conclude that the trap density decreases after recrystallization as the improved crystallinity and the enlarged grains lead to fewer defects in the bulk and at the GBs.

V. SPATIALLY RESOLVED CONDUCTIVITY

To further understand the defects and spatially resolved electronic properties, we measured the local current by conductive atomic force microscopy (c-AFM). Figures 5(a)–5(c) show the topology of the non-treated and MA⁰ treated perovskite films. While the reference perovskite film features the typical small crystallites with grain sizes in the range of a few hundred nanometers, the MA⁰ treated films exhibit domains with sizes exceeding several tens of micrometers. The MA⁰ treated perovskite films also show a smaller root mean square roughness (16 nm for both 80 and 90 °C samples) than the non-treated counterparts (18.21 nm).

c-AFM maps of the three perovskite films [Figs. 5(d)–5(f)] show clear differences in the local electronic properties. A comparison of spatial surface current maps of perovskite films measured in the dark and under illumination (Figs. S14–S21) shows a manifold increase in current upon illumination. Note that the light intensity that was applied to the reference perovskite films saturates the current value when illuminating the MA⁰ treated perovskite films. Therefore, lower intensities were used in the measurements of the

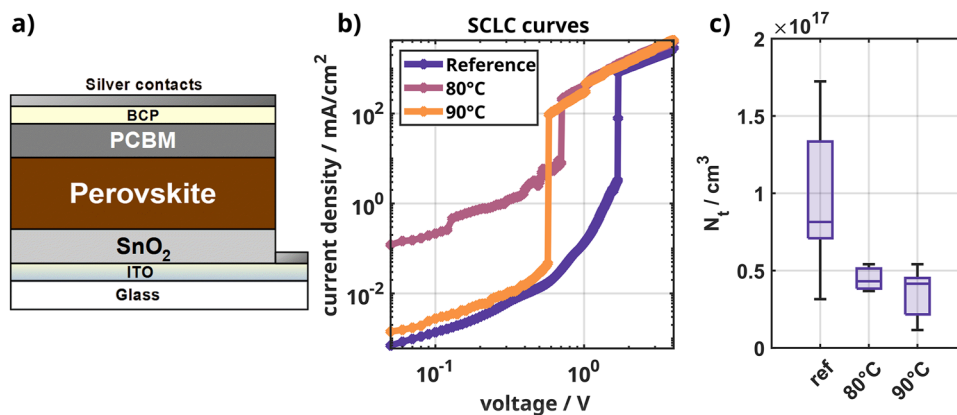


FIG. 4. (a) Architecture of the electron-only devices used for SCLC measurements. (b) Exemplary SCLC J - V curves of the reference device and MA⁰ treated devices after recrystallization at 80 and 90 °C. It is apparent that the V_{TFL} shifts to lower voltages in the MA⁰ treated films. (c) Extracted electron trap densities for the three types of devices.

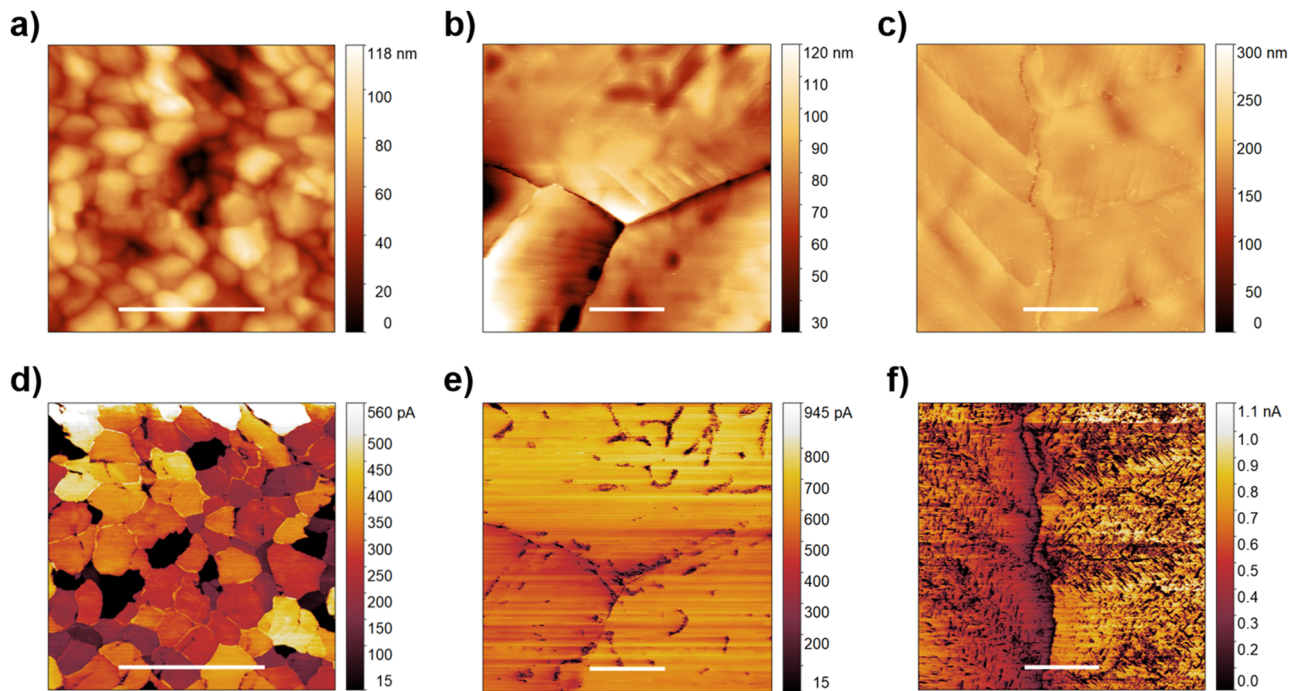


FIG. 5. (a)–(c) AFM topographies of the reference sample (scale bar $1\ \mu\text{m}$) as well as the 80 and 90 °C MA^0 treated samples (scale bars $5\ \mu\text{m}$), respectively. (d)–(f) Corresponding c-AFM maps under illumination of the reference sample as well as the 80 and 90 °C MA^0 treated samples.

recrystallized films. Clearly, the MA^0 treated perovskite films show a significantly higher local current than their non-treated reference counterpart, despite much lower illumination intensities. After recrystallization, the films exhibit a lower defect density, leading to a less recombination and, thus, a higher current. The 90 °C perovskite film shows the highest spatial current, which is indicative of the highest surface conductivity.

Another notable feature in the c-AFM maps of three films is the presence of distinct dark regions in the reference perovskite film, which is attributed to non-perovskite lead(II) iodide (PbI_2) phases that can be formed during the annealing process.^{59,60} These features are absent in the recrystallized films, suggesting an improved spatial homogeneity.

Both the 80 and 90 °C perovskite films show a drop in current at the GBs. Notably, the current in the 90 °C sample drops at the distinct crack-like GB, but not at the line-like features within the large perovskite domains (see Fig. S22, profiles 3 and 4). This suggests that not all visible boundaries are equivalent and only some of them are detrimental for charge transport across the perovskite film.

In contrast to the MA^0 treated films, we note a *higher* current at the GBs in the reference perovskite film (Fig. S20). The c-AFM image of the same sample in the dark does not show this trend, suggesting that this effect is related to charge accumulation. Similar observations of higher currents at the GBs have been made in several publications.^{61–63} It was suggested that the GBs act as effective charge dissociation centers when an applied bias overcomes the barrier height created by the boundary. A higher spatial current at the GB

compared to within the grain has also been experimentally demonstrated in a previous report,⁶⁴ suggesting that the defects formed were shallow in nature and play a beneficial role in charge transport. The different spatial surface current profiles of non-treated vs MA^0 treated perovskite films suggest that charge carriers dissociate at the GBs in the former, while efficient charge dissociation and transport take place within the grains in the latter.

VI. APPLICATION IN PHOTODETECTORS

To investigate how these improvements in the film structure translate to the performance of non-treated vs MA^0 treated perovskite films in device applications, photodetectors were fabricated in the configuration ITO/ SnO_2 /perovskite/molybdenum trioxide (MoO_3) (10 nm)/gold (Au) (100 nm). Figures 6(a)–6(c) show the current–voltage (I – V) curves of the three devices at various illumination intensities. It is evident that the photocurrent increases with the illumination intensity. The maximum values at $350\ \text{mW cm}^{-2}$ and a bias of 2 V are 82 and 75 nA for the 80 and 90 °C samples, respectively. The current passing through the reference device is much smaller (2 nA) under the same measurement conditions. We further note that the magnitudes of the current increase under illumination (on/off ratio) are 18, 260, and 230 for the reference, 80, and 90 °C samples, respectively. It is, therefore, an order of magnitude higher for the MA^0 treated samples, with the 80 °C samples showing the most pronounced increase. We attribute the higher currents and on/off ratios of the MA^0 treated samples to the lower defect density.

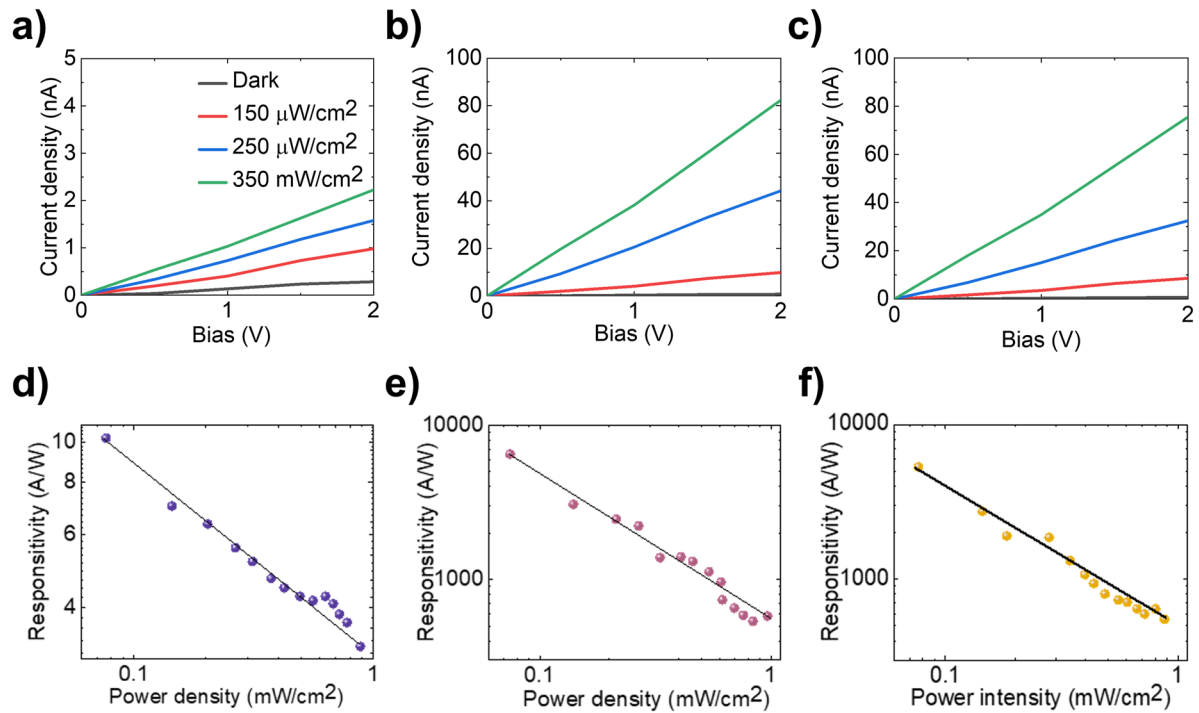


FIG. 6. (a)–(c) Photocurrent response of the three devices [reference in (a), 80 °C in (b), and 90 °C in (b)] at various excitation power densities and applied biases under 515 nm laser irradiation. (d)–(f) Responsivity as a function of power density of the reference in (d), 80 °C in (e), and 90 °C in (f) at 1 V.

In Figs. 6(d)–6(f), the responsivities are plotted over the power density, with the best performing device (MA⁰ treated at 80 °C) demonstrating a responsivity of about 580 A W⁻¹ at 1 mW cm⁻², which is nearly 200 times higher than the reference device (3 A W⁻¹ at 1 mW cm⁻²). The device MA⁰ treated at 90 °C also demonstrated a similar responsivity value of 551 A W⁻¹ at 1 mW cm⁻² (under 515 nm laser illumination). The detectivity is a further important parameter to characterize the performance of photodetectors. The specific detectivity is given by⁴

$$D^* = A^{1/2} \cdot \frac{R}{(2 \cdot e \cdot I_{\text{dark}})^{1/2}}, \quad (3)$$

where A corresponds to the device area, R is the responsivity, e denotes the elementary charge, and I_{dark} refers to the dark current passing through the device. The specific detectivities of both MA⁰ treated devices at 80 and 90 °C are 4.19×10^{11} and 3.94×10^{11} Jones, respectively, which are about two orders of magnitude higher than that of the non-treated reference device ($D^* = 3.36 \times 10^9$ Jones). Further important characteristics of photodetectors are the rise and fall times, which are directly related to the trap distribution in the perovskite films (in the bulk or at the surface). The rise time refers to the time required for the photodetector to rise from 10% to 90% of its full photocurrent value upon illumination. Analogously, the fall time is the time it takes for the photocurrent to drop from 90% to 10% when the laser is switched off. As shown in Figs. 7(a)–7(c), the rise and fall times for the MA⁰ treated devices are in the range of a few

microseconds. In contrast, the response times of the reference films are several orders of magnitude longer (≈ 0.1 s). Such a significant increase in the response time of the MA⁰ treated perovskite films, despite the similar device architecture, shows the beneficial effect of the reduced defect density after MA⁰ treatment. The possibility of electron trapping and de-trapping at the defect sites is lowered, increasing the rise/fall times drastically.

Finally, Figs. 7(d)–7(f) show the normalized responsivity as a function of the laser modulation frequency. These figures illustrate that the 3 dB bandwidth for the MA⁰ treated perovskite film-based photodetectors is above 450 kHz, which is significantly higher than the reference device (0.25 kHz). Notably, the 90 °C device shows a higher speed compared to the 80 °C device despite the lower sensitivity of the former, which could be beneficial for low-power, high-bandwidth on-chip interconnects in integrated electronics. Note that although only selected devices are shown here, the results have proven to be very reproducible across multiple films and devices.

In conclusion, the photodetectors employing MA⁰ treated perovskite films show significantly better device performances than the non-treated reference devices. We believe this enhanced performance is due to two reasons: First, the larger grain size and low trap density (calculated from the SCLC measurement) of the MA⁰ treated perovskite morphologies, and second, a lower trap filling effect in the MA⁰ treated films as compared to a reference non-treated perovskite film, as evidenced in our TRPL data and the comparison of the rise/fall times.

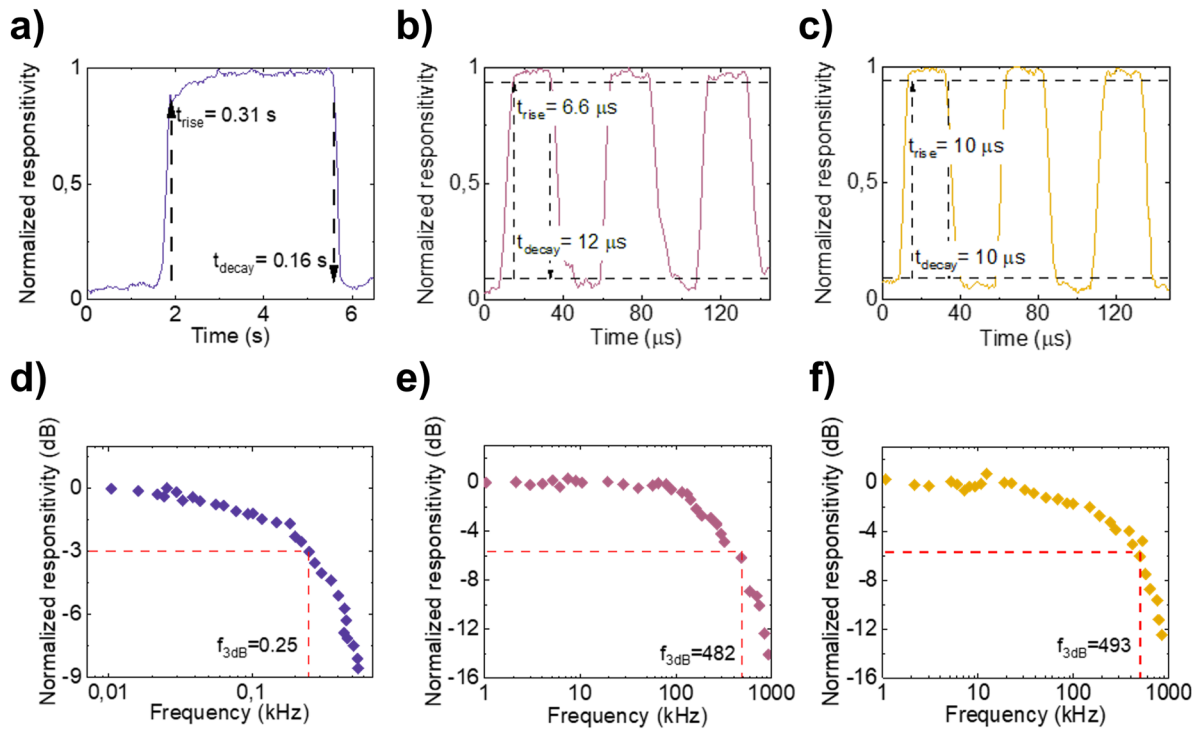


FIG. 7. (a)–(c) The rise and fall times of the three perovskite photodetectors [reference in (a), 80 °C in (b), and 90 °C in (c)] at 2 V. The incident laser light was switched on and off with a frequency of 0.125 and 15 kHz for the reference and MA⁰ treated devices, respectively. (d)–(f) The normalized responsivity as a function of frequency at 2 V for the reference sample in (d), the 80 °C in (e), and 90 °C in (f) samples.

VII. CONCLUSION

In this work, we present a MA⁰ treatment protocol for the reliable and adaptable fabrication of highly crystalline perovskite films. By recrystallizing samples under MA⁰ atmosphere at elevated temperatures, we achieve large domains of uniform orientation. In consequence, the MA⁰ treatment results in significantly increased crystallinities. XRD studies also show a peak shift, which we attribute to the exchange of FA⁺ for MA⁺ in the lattice of the mixed-cation perovskite with an additional strain-induced component. The implications of this change in compositions are unclear, but it could be prevented by replacing MA⁰ with another amine, such as ammonia,⁶⁵ which cannot be permanently integrated into the perovskite structure. PL studies show that light-soaking induced defect-curing is reduced after MA⁰ treatment, indicating a decreased trap density, which was confirmed by SCLC measurements. Through c-AFM measurements, we show that this improvement results in a higher conductivity and a lower charge accumulation at the grain boundaries, indicating efficient charge dissociation and transport within the grains.

Finally, we demonstrate that these properties translate into strongly improved detectivities and response times when applied in photodetection devices. The use of such MA⁰ treatments could be highly beneficial for future applications, e.g., for the further development of perovskite-based photodetectors and perovskite solar cells,

where a low trap density is a prerequisite to achieving highly efficient and stable devices.

VIII. METHODS

Sample fabrication. All samples were prepared on Lumtec ITO glass sheets. Prior to layer deposition, the substrates were cleaned in an ultrasonic bath for 30 min each in deionized (DI) water with detergent, DI water, acetone and isopropanol, respectively. This was followed by 7 min oxygen plasma treatment. The SnO₂ precursor was prepared via the reflux method,⁶⁶ which involves heating a 0.1M solution of tin(II) chloride dihydrate (SnCl₂ · 2H₂O) (*Alfa Aesar*) in a 1:19 mixture of butanol (*Sigma-Aldrich*) and DI water at 110 °C for 4 h. SnO₂ layers were obtained via spin-coating the mixture solution at 2000 rpm for 30 s and annealing for 60 min at 130 °C. For the perovskite precursor, 507.1 mg of PbI₂ (*TCI*) and 73.4 mg lead(II) bromide (PbBr₂) (*Sigma-Aldrich*) were dissolved in 1 ml 1:4 dimethyl sulfoxide (DMSO):*N,N*-dimethylformamide (DMF) (both anhydrous, *Sigma-Aldrich*). This solution was used to additionally dissolve 22.4 mg methylammonium bromide (MaBr) (*Sigma-Aldrich*) and 172 mg formamidinium iodide (FAI) (*Great-cell Solar*). Finally, 53 μl of 389.7 mg ml⁻¹ cesium iodide (CsI) (*Sigma-Aldrich*) in DMSO was added. The precursor was spin-coated at 1000 rpm for 10 s and then at 6000 rpm for 20 s.

250 μl of chlorobenzene (CB) (anhydrous, *Sigma-Aldrich*) was dropped onto the sample roughly 5 s before the end of the program as anti-solvent, and the sample was transferred onto a hotplate at 100 °C for 60 min annealing.

The MA⁰ treatment was performed with a MA⁰ partial pressure of 230 mbar during exposure. The film was kept under this atmosphere for 10 s before pumping to $p_0 = 600$ mbar, thus reducing the MA⁰ partial pressure to roughly 170 mbar during recrystallization. See the [supplementary material](#) for more details. The process was observed from above with a *DinoLite AF4915ZTL* microscope camera. To measure the recrystallization temperatures shown in [Fig. 1\(a\)](#), untreated triple-cation perovskite films were exposed to a fixed MA⁰ partial pressure p_{MA} at different temperatures, until the highest temperature at which the film still turned into the transparent liquid was found and determined to be T_{rec} .

The electron-only devices for SCLC measurements were finalized by spin-coating 20 mg ml⁻¹ [60]-PCBM (99% purity, *Ossila*) in CB (*Sigma-Aldrich*) at 2000 rpm for 90 s, annealing at 70 °C for 10 min, and spin-coating 0.5 mg ml⁻¹ BCP in ethanol (anhydrous, *Sigma-Aldrich*) for 30 s at 5000 rpm. Finally, a 100 nm thick Ag contact layer was evaporated. For photodetectors, 10 nm of MoO₃ followed by 100 nm of Au was evaporated on top of the perovskite layers. All film deposition steps (except the initial SnO₂ layer), contact evaporation, and the SCLC characterization were performed in inert nitrogen atmosphere.

Characterization. SEM imaging and electron backscatter diffraction (EBSD) studies were performed on a Zeiss Gemini 500 electron microscope. XRD measurements were performed on a *Bruker D8* x-ray diffractometer. The XPS analyses were carried out in a Thermo Scientific Multilab 2000 spectrometer fitted with a dual-anode x-ray source (Mg K alpha and Al K alpha with photon energies 1253.6 and 1486.7 eV, respectively) and a 110 mm hemispherical sector analyzer. Survey spectra and high resolution core level spectra were measured using the Mg k-alpha x-ray source at 400 W and 15 eV pass energy. Each sample was supported on a sample stub using a copper double adhesive tape before entering to FEAL chamber. All the measurements were made on as-received samples and no surface sputtering with Ar ions was done. The core level spectra were fitted and deconvoluted using the CASA XPS software package. PL and TRPL were measured on a *PicoQuant FluTime300* fluorescence spectrometer using a 405 nm excitation laser. The repetition rate was set to 40 MHz for steady state- and 1 MHz for time-resolved measurements. To block stray laser light, a 455 nm longpass filter was placed between the sample and the detector. For long-term illumination, the steady state settings were used. UV-vis absorbance spectroscopy was performed with a CARY 5000 UV/Vis spectrometer by Agilent Technologies. The conductive AFM measurements were carried out using a MFP-3D infinity atomic force microscope from Asylum Research (Oxford Instruments) in a nitrogen filled glovebox where the humidity and the oxygen levels are below 0.4% and 0.1%, respectively. The conductive AFM was performed with the platinum-iridium coated SCM PIT-V2 cantilevers (*Bruker*) with spring constants of 3 mN nm⁻¹ and a free resonance of 75 kHz. The cantilever holder for the conductive AFM measurement was an ORCA cantilever holder from Asylum Research with 2 nA N⁻¹ current amplification factor. The applied voltage was 750 mV for each sample. The photocurrent measurements were performed via an external light source with an adjustable light intensity. Photodetector

characterization was performed using a probe station under ambient condition. A red light-emitting diode (LED) (*OVLBx4C7 Series*, *OPTEK Technology, Inc.*, main wavelength: 514 nm) was mounted above the photodetector, which was controlled by a *Keysight B2902A* precision source/measure unit in the current source mode. The optical power density that reached the sample surface was determined by measuring a commercial reference photodiode (*PDB-C154SM*, *Luna Optoelectronics*) with a responsivity of ≈ 0.3 A W⁻¹ at 514 nm.

SUPPLEMENTARY MATERIAL

See the [supplementary material](#) for more details on the MA⁰ treatment process and process pressures, further structural characterization, further PL and UV-vis absorbance measurements, the Williamson-Hall analysis, XPS measurements, and more detailed AFM and c-AFM maps.

ACKNOWLEDGMENTS

E.R.S., T.S., L.S.-M., Y.Y., and S.A.L.W. acknowledge the SPP2196 Project (Deutsche Forschungsgemeinschaft, DFG) for funding. This study was supported by Ministry of Science and ICT through the National Research Foundation grant, funded by the Korea Government (Grant No. 2020R1A4A1019455).

AUTHOR DECLARATIONS

Conflict of Interest

The authors have no conflicts to disclose.

Author Contributions

Emilia R. Schütz: Conceptualization (equal); Data curation (lead); Investigation (equal). **Azhar Fakharruddin:** Conceptualization (equal); Investigation (equal); Supervision (equal). **Yenal Yalcinkaya:** Data curation (supporting). **Efrain Ochoa-Martinez:** Data curation (supporting). **Shanti Bijani:** Data curation (supporting). **Abd. Rashid bin Mohd Yusoff:** Data curation (supporting). **Maria Vasilopoulou:** Data curation (supporting). **Tobias Seewald:** Data curation (equal); Investigation (equal). **Ullrich Steiner:** Project administration (supporting). **Stefan A. L. Weber:** Project administration (supporting); Supervision (supporting). **Lukas Schmidt-Mende:** Conceptualization (equal); Project administration (equal); Resources (lead); Supervision (lead).

DATA AVAILABILITY

The data that support the findings of this study are available from the corresponding author upon reasonable request.

REFERENCES

- ¹P. Roy, N. Kumar Sinha, S. Tiwari, and A. Khare, *Solar Energy* **198**, 665 (2020).
- ²X.-K. Liu, W. Xu, S. Bai, Y. Jin, J. Wang, R. H. Friend, and F. Gao, *Nat. Mater.* **20**, 10 (2021).

- ³L. Basiricò, A. Ciavatti, and B. Fraboni, *Adv. Mater. Technol.* **6**, 2000475 (2021).
- ⁴C. Xie, C. K. Liu, H. L. Loi, and F. Yan, *Adv. Funct. Mater.* **30**, 1903907 (2020).
- ⁵K. X. Steirer, P. Schulz, G. Teeter, V. Stevanovic, M. Yang, K. Zhu, and J. J. Berry, *ACS Energy Lett.* **1**, 360 (2016).
- ⁶D. Meggiolaro, S. G. Motti, E. Mosconi, A. J. Barker, J. Ball, C. Andrea Riccardo Perini, F. Deschler, A. Petrozza, and F. De Angelis, *Energy Environ. Sci.* **11**, 702 (2018).
- ⁷X. Zhang, M. E. Turiansky, and C. G. Van de Walle, *J. Phys. Chem. C* **124**, 6022 (2020).
- ⁸J. H. Noh, S. H. Im, J. H. Heo, T. N. Mandal, and S. I. Seok, *Nano Lett.* **13**, 1764 (2013).
- ⁹A. Amat, E. Mosconi, E. Ronca, C. Quarti, P. Umari, M. K. Nazeeruddin, M. Grätzel, and F. De Angelis, *Nano Lett.* **14**, 3608 (2014).
- ¹⁰G. E. Eperon, S. D. Stranks, C. Menelaou, M. B. Johnston, L. M. Herz, and H. J. Snaith, *Energy Environ. Sci.* **7**, 982 (2014).
- ¹¹A. Ummadisingu, S. Meloni, A. Mattoni, W. Tress, and M. Grätzel, *Angew. Chem., Int. Ed.* **60**, 21368 (2021).
- ¹²C. Wehrenfennig, G. E. Eperon, M. B. Johnston, H. J. Snaith, and L. M. Herz, *Adv. Mater.* **26**, 1584 (2014).
- ¹³H. Oga, A. Saeki, Y. Ogomi, S. Hayase, and S. Seki, *J. Am. Chem. Soc.* **136**, 13818 (2014).
- ¹⁴Z. Fan, K. Sun, and J. Wang, *J. Mater. Chem. A* **3**, 18809 (2015).
- ¹⁵A. Dubey, N. Adhikari, S. Mabrouk, F. Wu, K. Chen, S. Yang, and Q. Qiao, *J. Mater. Chem. A* **6**, 2406 (2018).
- ¹⁶S. Sánchez, L. Pfeifer, N. Vlachopoulos, and A. Hagfeldt, *Chem. Soc. Rev.* **50**, 7108 (2021).
- ¹⁷F. Wang, S. Bai, W. Tress, A. Hagfeldt, and F. Gao, *npj Flexible Electron.* **2**, 22 (2018).
- ¹⁸Y. Lei, Y. Xu, M. Wang, G. Zhu, and Z. Jin, *Small* **17**, 2005495 (2021).
- ¹⁹E. Aydin, M. De Bastiani, and S. De Wolf, *Adv. Mater.* **31**, 1900428 (2019).
- ²⁰A.-F. Castro-Méndez, J. Hidalgo, and J.-P. Correa-Baena, *Adv. Energy Mater.* **9**, 1901489 (2019).
- ²¹N. Phung and A. Abate, *Small* **14**, 1802573 (2018).
- ²²W. Nie, H. Tsai, R. Asadpour, J.-C. Blancon, A. J. Neukirch, G. Gupta, J. J. Crochet, M. Chhowalla, S. Tretiak, M. A. Alam, H.-L. Wang, and A. D. Mohite, *Science* **347**, 522 (2015).
- ²³K. Liao, C. Li, L. Xie, Y. Yuan, S. Wang, Z. Cao, L. Ding, and F. Hao, *Nano-Micro Lett.* **12**, 156 (2020).
- ²⁴X. Ren, Z. Yang, D. Yang, X. Zhang, D. Cui, Y. Liu, Q. Wei, H. Fan, and S. F. Liu, *Nanoscale* **8**, 3816 (2016).
- ²⁵Z. Yang, Y. Deng, X. Zhang, S. Wang, H. Chen, S. Yang, J. Khurgin, N. X. Fang, X. Zhang, and R. Ma, *Adv. Mater.* **30**, 1704333 (2018).
- ²⁶Z. Li, X. Liu, C. Zuo, W. Yang, and X. Fang, *Adv. Mater.* **33**, 2103010 (2021).
- ²⁷P. Shi, Y. Ding, Y. Ren, X. Shi, Z. Arain, C. Liu, X. Liu, M. Cai, G. Cao, M. K. Nazeeruddin, and S. Dai, *Adv. Sci.* **6**, 1901591 (2019).
- ²⁸Z. Yang, Q. Xu, X. Wang, J. Lu, H. Wang, F. Li, L. Zhang, G. Hu, and C. Pan, *Adv. Mater.* **30**, 1802110 (2018).
- ²⁹F. Zhang, J. Song, L. Zhang, F. Niu, Y. Hao, P. Zeng, H. Niu, J. Huang, and J. Lian, *J. Mater. Chem. A* **4**, 8554 (2016).
- ³⁰M. Hu, C. Bi, Y. Yuan, Y. Bai, and J. Huang, *Adv. Sci.* **3**, 1500301 (2016).
- ³¹Q. Lian, M. Z. Mokhtar, D. Lu, M. Zhu, J. Jacobs, A. B. Foster, A. G. Thomas, B. F. Spencer, S. Wu, C. Liu, N. W. Hodson, B. Smith, A. Alkaltham, O. M. Alkudhari, T. Watson, and B. R. Saunders, *ACS Appl. Mater. Interfaces* **12**, 18578 (2020).
- ³²T. Seewald, E. R. Schütz, C. Ebenhoch, and L. Schmidt-Mende, *J. Phys.: Energy* **2**, 021001 (2020).
- ³³Z. Zhou, Z. Wang, Y. Zhou, S. Pang, D. Wang, H. Xu, Z. Liu, N. P. Padture, and G. Cui, *Angew. Chem., Int. Ed.* **54**, 9705 (2015).
- ³⁴S. R. Raga, Y. Jiang, L. K. Ono, and Y. Qi, *Energy Technol.* **5**, 1750 (2017).
- ³⁵D. Bogachuk, L. Wagner, S. Mastroianni, M. Daub, H. Hillebrecht, and A. Hinsch, *J. Mater. Chem. A* **8**, 9788 (2020).
- ³⁶X. Huang, R. Chen, G. Deng, F. Han, P. Ruan, F. Cheng, J. Yin, B. Wu, and N. Zheng, *J. Am. Chem. Soc.* **142**, 6149 (2020).
- ³⁷Y. Jiang, E. J. Juarez-Perez, Q. Ge, S. Wang, M. R. Leyden, L. K. Ono, S. R. Raga, J. Hu, and Y. Qi, *Mater. Horiz.* **3**, 548 (2016).
- ³⁸D. L. Jacobs and L. Zang, *Chem. Commun.* **52**, 10743 (2016).
- ³⁹H. Fan, F. Li, P. Wang, Z. Gu, J.-H. Huang, K.-J. Jiang, B. Guan, L.-M. Yang, X. Zhou, and Y. Song, *Nat. Commun.* **11**, 5402 (2020).
- ⁴⁰A. Günzler, E. Bermúdez-Ureña, L. A. Muscarella, M. Ochoa, E. Ochoa-Martínez, B. Ehrler, M. Saliba, and U. Steiner, *ACS Appl. Mater. Interfaces* **13**, 6854 (2021).
- ⁴¹G. E. Eperon, V. M. Burlakov, P. Docampo, A. Goriely, and H. J. Snaith, *Adv. Funct. Mater.* **24**, 151 (2014).
- ⁴²C. Zhu, X. Niu, Y. Fu, N. Li, C. Hu, Y. Chen, X. He, G. Na, P. Liu, H. Zai, Y. Ge, Y. Lu, X. Ke, Y. Bai, S. Yang, P. Chen, Y. Li, M. Sui, L. Zhang, H. Zhou, and Q. Chen, *Nat. Commun.* **10**, 815 (2019).
- ⁴³G. E. Eperon, D. Bryant, J. Troughton, S. D. Stranks, M. B. Johnston, T. Watson, D. A. Worsley, and H. J. Snaith, *J. Phys. Chem. Lett.* **6**, 129 (2015).
- ⁴⁴Z. Zhao, F. Gu, Y. Li, W. Sun, S. Ye, H. Rao, Z. Liu, Z. Bian, and C. Huang, *Adv. Sci.* **4**, 1700204 (2017).
- ⁴⁵Y. Zong, Y. Zhou, M. Ju, H. F. Garces, A. R. Krause, F. Ji, G. Cui, X. C. Zeng, N. P. Padture, and S. Pang, *Angew. Chem., Int. Ed.* **55**, 14723 (2016).
- ⁴⁶Y. Zhou, M. Yang, S. Pang, K. Zhu, and N. P. Padture, *J. Am. Chem. Soc.* **138**, 5535 (2016).
- ⁴⁷S. Pang, Y. Zhou, Z. Wang, M. Yang, A. R. Krause, Z. Zhou, K. Zhu, N. P. Padture, and G. Cui, *J. Am. Chem. Soc.* **138**, 750 (2016).
- ⁴⁸C. Li, Y. Zhong, C. A. M. Luna, T. Unger, K. Deichsel, A. Gräser, J. Köhler, A. Köhler, R. Hildner, and S. Huettner, *Molecules* **21**, 1081 (2016).
- ⁴⁹S. Ghosh, S. K. Pal, K. J. Karki, and T. Pullerits, *ACS Energy Lett.* **2**, 2133 (2017).
- ⁵⁰D. W. deQuilettes, W. Zhang, V. M. Burlakov, D. J. Graham, T. Leijtens, A. Osherov, V. Bulović, H. J. Snaith, D. S. Ginger, and S. D. Stranks, *Nat. Commun.* **7**, 11683 (2016).
- ⁵¹Y. Tian, M. Peter, E. Unger, M. Abdellah, K. Zheng, T. Pullerits, A. Yartsev, V. Sundström, and I. G. Scheblykin, *Phys. Chem. Chem. Phys.* **17**, 24978 (2015).
- ⁵²Y. Tian, A. Merdasa, E. Unger, M. Abdellah, K. Zheng, S. McKibbin, A. Mikkelsen, T. Pullerits, A. Yartsev, V. Sundström, and I. G. Scheblykin, *J. Phys. Chem. Lett.* **6**, 4171 (2015).
- ⁵³X. Fu, D. A. Jacobs, F. J. Beck, T. Duong, H. Shen, K. R. Catchpole, and T. P. White, *Phys. Chem. Chem. Phys.* **18**, 22557 (2016).
- ⁵⁴K. Handloser, N. Giesbrecht, T. Bein, P. Docampo, M. Handloser, and A. Hartschuh, *ACS Photonics* **3**, 255 (2016).
- ⁵⁵M. A. Lampert, *Phys. Rev.* **103**, 1648 (1956).
- ⁵⁶M. A. Lampert and P. Mark, *Current Injection in Solids* (Academic Press, 1970).
- ⁵⁷Q. Lin, A. Armin, R. C. R. Nagiri, P. L. Burn, and P. Meredith, *Nat. Photonics* **9**, 106 (2015).
- ⁵⁸H. S. Jung and N.-G. Park, *Small* **11**, 10 (2015).
- ⁵⁹Q. Chen, H. Zhou, T.-B. Song, S. Luo, Z. Hong, H.-S. Duan, L. Dou, Y. Liu, and Y. Yang, *Nano Lett.* **14**, 4158 (2014).
- ⁶⁰S. Gharibzadeh, P. Fassel, I. M. Hossain, P. Rohrbeck, M. Frericks, M. Schmidt, T. Duong, M. R. Khan, T. Abzieher, B. A. Nejang, F. Schackmar, O. Almora, T. Feeney, R. Singh, D. Fuchs, U. Lemmer, J. P. Hofmann, S. A. L. Weber, and U. W. Paetzold, *Energy Environ. Sci.* **14**, 5875 (2021).
- ⁶¹J.-J. Li, J.-Y. Ma, Q.-Q. Ge, J.-S. Hu, D. Wang, and L.-J. Wan, *ACS Appl. Mater. Interfaces* **7**, 28518 (2015).
- ⁶²J. S. Yun, A. Ho-Baillie, S. Huang, S. H. Woo, Y. Heo, J. Seidel, F. Huang, Y.-B. Cheng, and M. A. Green, *J. Phys. Chem. Lett.* **6**, 875 (2015).
- ⁶³Y. Kutes, Y. Zhou, J. L. Bosse, J. Steffes, N. P. Padture, and B. D. Huey, *Nano Lett.* **16**, 3434 (2016).
- ⁶⁴J. Song, Y. Zhou, N. P. Padture, and B. D. Huey, *Nat. Commun.* **11**, 3308 (2020).
- ⁶⁵X. Y. Feng, K. W. Ng, S. P. Wang, W. Z. Chen, Z. Z. Zhang, W. Chen, Y. Y. Zhao, B. Tu, Z. K. Tang, H. Pan, and Z. B. He, *J. Mater. Chem. A* **8**, 13585 (2020).
- ⁶⁶C. Chen, Y. Jiang, J. Guo, X. Wu, W. Zhang, S. Wu, X. Gao, X. Hu, Q. Wang, G. Zhou, Y. Chen, J. M. Liu, K. Kempa, and J. Gao, *Adv. Funct. Mater.* **29**, 1900557 (2019).